Monthly Notices of the ROYAL ASTRONOMICAL SOCIETY

MNRAS **474,** 1398–1411 (2018) doi:10.1093/mnras/stx2855
Advance Access publication 2017 November 3

The core–cusp problem: a matter of perspective

Anna Genina,[1⋆] Alejandro Benítez-Llambay,[1⋆] Carlos S. Frenk,[1] Shaun Cole,[1] Azadeh Fattahi,[1] Julio F. Navarro,[2†] Kyle A. Oman,[2] Till Sawala[3] and Tom Theuns[1]

[1]*Institute for Computational Cosmology, Department of Physics, Durham University, South Road, Durham DH1 3LE, UK*
[2]*Department of Physics & Astronomy, University of Victoria, Victoria BC, V8P 5C2, Canada*
[3]*Department of Physics, University of Helsinki, Gustaf Hällströmin katu 2a, FI-00014 Helsinki, Finland*

Accepted 2017 November 1. Received 2017 October 9; in original form 2017 July 20

ABSTRACT

The existence of two kinematically and chemically distinct stellar subpopulations in the Sculptor and Fornax dwarf galaxies offers the opportunity to constrain the density profile of their matter haloes by measuring the mass contained within the well-separated half-light radii of the two metallicity subpopulations. Walker and Peñarrubia have used this approach to argue that data for these galaxies are consistent with constant-density 'cores' in their inner regions and rule out 'cuspy' Navarro–Frenk–White (NFW) profiles with high statistical significance, particularly in the case of Sculptor. We test the validity of these claims using dwarf galaxies in the APOSTLE (A Project Of Simulating The Local Environment) Λ cold dark matter cosmological hydrodynamic simulations of analogues of the Local Group. These galaxies all have NFW dark matter density profiles and a subset of them develop two distinct metallicity subpopulations reminiscent of Sculptor and Fornax. We apply a method analogous to that of Walker and Peñarrubia to a sample of 50 simulated dwarfs and find that this procedure often leads to a statistically significant detection of a core in the profile when in reality there is a cusp. Although multiple factors contribute to these failures, the main cause is a violation of the assumption of spherical symmetry upon which the mass estimators are based. The stellar populations of the simulated dwarfs tend to be significantly elongated and, in several cases, the two metallicity populations have different asphericity and are misaligned. As a result, a wide range of slopes of the density profile are inferred depending on the angle from which the galaxy is viewed.

Key words: galaxies: dwarf – galaxies: formation – galaxies: kinematics and dynamics – dark matter.

1 INTRODUCTION

One of the fundamental predictions of the Λ cold dark matter (ΛCDM) model of cosmogony is that dark matter assembles into haloes that, in the absence of baryon effects, develop steeply rising inner radial density profiles, or cusps. This important result was obtained from *N*-body simulations which showed that the density distribution of a dark matter halo of any mass is well fitted by a Navarro–Frenk–White profile (NFW; Navarro, Eke & Frenk 1996; Navarro, Frenk & White 1997) independently of initial conditions and cosmological parameters.

The inner slope of the NFW profile follows $\rho \propto r^{-1}$. In contrast, measurements of galaxy rotation curves and dynamical models of dwarf spheroidal galaxies are often claimed to require shallower density profile slopes that are consistent with a constant-density core at the centre, $\rho \propto r^{0}$ (e.g. Flores & Primack 1994; Moore 1994; Battaglia et al. 2008; Walker & Peñarrubia 2011; Agnello & Evans 2012; Amorisco & Evans 2012; Adams et al. 2014; Oh et al. 2015). This disagreement between observations and simulations has become known as the *core-cusp problem*.

In order to resolve this discrepancy, a number of mechanisms involving baryons, which could transform cusps into cores, have been proposed. For example, cores may be created when baryons, after slowly condensing at the centre of a halo, are suddenly expelled by supernova feedback, either in a single event (Navarro et al. 1996; Read & Gilmore 2005) or through repeated episodes of star formation (Pontzen & Governato 2012; Brooks & Zolotov 2014). Alternatively, energy could be transferred to the outer halo by clumps infalling due to dynamical friction (El-Zant, Shlosman & Hoffman 2001; Sánchez-Salcedo, Reyes-Iturbide & Hernandez 2006; Mashchenko, Wadsley & Couchman 2008;

⋆ E-mail: anna.genina@durham.ac.uk (AG); alejandro.b.llambay@durham.ac.uk (AB-L)
† Senior CIfAR Fellow.

Del Popolo & Kroupa 2009; Cole, Dehnen & Wilkinson 2011), or through resonant effects induced by a central stellar bar (Weinberg & Katz 2002).

Dwarf spheroidal galaxies are promising objects to test ideas about the inner structure of dark matter haloes. These galaxies are strongly dark-matter dominated (Pryor & Kormendy 1990) and, although they are faint, some are sufficiently close-by that their stellar populations can be resolved. Much effort has therefore been invested in trying to infer their halo profiles. A large body of work is concerned with field galaxies with measurable H I velocity fields; many such studies claim robust detections of central cores (e.g. Kuzio de Naray et al. 2006; Oh et al. 2011; Adams et al. 2014). However, a recent study (Oman et al. 2017), based on the same APOSTLE (A Project Of Simulating The Local Environment) simulations that we will analyse here, has revealed the presence of systematic effects in even the most detailed analyses of spatially resolved kinematics, casting doubt on claims that cores are present in those galaxies. Similar conclusions were reached by Pineda et al. (2017).

The kinematics of resolved stars in nearby galaxies offers an alternative to the kinematics of H I gas as a probe of the density structure of haloes. The detection of cores in several dwarf satellites of the Milky Way has been claimed on the basis of simple Jeans analyses (e.g. Gilmore et al. 2007), but the more general analysis by Strigari, Frenk & White (2010) has shown that current data are, in fact, unable to distinguish between cores and cusps in the Milky Way satellites. Some satellites of the Milky Way and Andromeda exhibit metallicity gradients: they have a centrally concentrated metal-rich population and a more extended, and kinematically hotter metal-poor population (Tolstoy et al. 2004; Battaglia et al. 2008, 2011). The origin of these systems is unknown but major mergers (Benítez-Llambay et al. 2016), reaccretion of gas (Tolstoy et al. 2004; Battaglia et al. 2006) or effects due to reionization (Kawata et al. 2006) have been proposed as possible origins of metallicity gradients.

The presence of two kinematically and spatially distinct metallicity components can be used to set constraints on the inner density profile of the common halo in which they move. Battaglia et al. (2008) identified a metal-rich ([Fe/H] > -1.5) and a metal-poor ([Fe/H] < -1.7) population in the Sculptor dwarf spheroidal and, using Jeans modelling, found that a wide range of profiles are consistent with the data, from a pseudo-isothermal sphere ($\rho \propto r^0$ at the centre) to an NFW profile. Amorisco & Evans (2012) pointed out that some of those models are unphysical and, fitting the Sculptor data to a particular phase-space distribution function, found that while a profile with a core is preferred by their χ^2 fits, an NFW profile is also allowed by the data. Using more general phase-space distribution functions, Strigari, Frenk & White (2014) also showed that the two metallicity subpopulations in Sculptor are consistent with an NFW profile. A similar conclusion, using Schwarzschild modelling, was reached by Breddels et al. (2013) who found that a core profile is also allowed, while a cusp in Sculptor was found to be favoured by an analysis based on the fourth-order virial theorem by Richardson & Fairbairn (2014).

Walker & Peñarrubia (2011) took this idea further and developed a statistical methodology to distinguish the two metallicity subpopulations in Sculptor and Fornax. Making use of the interesting result of Wolf et al. (2010) and Walker et al. (2009) that the mass of a spherical stellar system in equilibrium can be robustly estimated at the half-mass radius of the system, they developed the method discussed in this paper and concluded that both Sculptor and Fornax have central cores, with Sculptor, in particular, ruling out an NFW profile at high statistical significance. Their method is based on estimating the total mass contained within the half-light radii of the metal-rich and metal-poor subpopulations, thus constraining the slope of the dark matter density profile. Wolf et al. (2010) and Walker et al. (2009) have argued that the mass within a characteristic radius of a collisionless spherical system in dynamical equilibrium is well constrained by the velocity dispersion and average radial distribution of a population of star tracers for a variety of stellar density and constant velocity anisotropy profiles.

Specifically, Wolf et al. (2010) showed that the mass is best constrained at radius, r_3, where the logarithmic slope of the stellar number density, $\mathrm{d}\log\nu/\mathrm{d}\log\mathrm{r}, = -3$, which is close to the deprojected half-light radius ($\frac{4}{3}R_\mathrm{e}$, where R_e is the projected half-light radius) for a range of stellar distributions. Their estimator is:

$$M\left(<\frac{4}{3}R_\mathrm{e}\right) = 4G^{-1}\langle\sigma_\mathrm{LOS}\rangle^2 R_\mathrm{e}, \tag{1}$$

where $\langle\sigma_\mathrm{LOS}\rangle$ is the *luminosity-averaged* line-of-sight velocity dispersion. Similarly, Walker et al. (2009) propose:

$$M\,(<R_\mathrm{e}) = \frac{5}{2}G^{-1}\langle\sigma_\mathrm{LOS}\rangle^2 R_\mathrm{e}. \tag{2}$$

Walker & Peñarrubia (2011) used a likelihood method to separate samples of stars in Sculptor and Fornax into two metallicity subcomponents and applied these mass estimators to each of them. For an object with mass density $\rho \propto r^{-\gamma}$, the enclosed mass is $M(r) \propto \frac{1}{3-\gamma}r^{3-\gamma}$. One can then define the asymptotic logarithmic mass slope as:

$$\Gamma = \lim_{\mathrm{r}\to 0}\left[\frac{d\log M}{d\log r}\right] = 3-\gamma. \tag{3}$$

For an NFW profile, the asymptotic inner slope is $\gamma = 1$, so $\Gamma = 2$, while for a core with $\gamma = 0$, $\Gamma = 3$. In the case of a galaxy with two segregated subpopulations, the two half-light radii will be located away from the centre and thus $\Gamma = \Delta\log M/\Delta\log r$ is a measure of the (steeper) density slope further out (Walker & Peñarrubia 2011). Assuming that the mass is given by the estimators above,

$$\Gamma \approx 1 + \frac{\log\left(\sigma_2^2/\sigma_1^2\right)}{\log\left(r_2/r_1\right)}, \tag{4}$$

where σ_i are the line-of-sight velocity dispersions and r_i are the half-light radii. Walker & Peñarrubia (2011) derived values of Γ for Sculptor and Fornax which exclude an NFW cusp at 99 and 96 per cent confidence levels, respectively, instead favouring a core. They argue that this conclusion is conservative because, if anything, the mass is likely to be overestimated for the central subpopulation.

In a recent paper Campbell et al. (2017) tested the accuracy of the mass estimators by applying them to galaxies in the APOSTLE hydrodynamic cosmological simulations of Local Group analogues (for which the true mass is known; see Section 2). They report little bias in the median mass estimates but a scatter of 25 and 23 per cent for the Walker et al. (2009) and Wolf et al. (2010) estimators, respectively, which are much larger than the values inferred by these authors from simulations of spherical systems in dynamical equilibrium. Campbell et al. (2017) find that a major contribution to the scatter comes from deviations from spherical symmetry which are quite common in simulated galaxies. Subsequently, Gonzalez-Samaniego et al. (2017) have generally confirmed the main conclusions of Campbell et al. (2017) regarding the scatter in the estimator from 12 dwarf galaxy analogues in the FIRE hydrodynamic simulations.

The effect of triaxality on Γ has been investigated by Laporte, Walker & Peñarrubia (2013a), who tagged dark matter particles

as stars in the (triaxial) dark matter haloes of the AQUARIUS simulations (Springel et al. 2008). These authors find that an anti-correlation between the measured half-light radius and the projected velocity dispersion acts to keep the mass estimate approximately constant, causing little variation in the derived value of Γ. However, by construction, the dark matter and the stars in their analysis have strongly correlated shapes (Laporte et al. 2013b) which can introduce a systematic effect.

Kowalczyk et al. (2013) carried out idealized *N*-body simulations of the evolution of dwarf spheroidal galaxies in the gravitational potential of a Milky-Way-like host. They introduced two spatially segregated disc subpopulations which evolve as the dwarf orbits in the halo of its host. They find that Γ may be over- or underestimated, depending on the line of sight. In particular, observations along the major axis of the dwarf tend to overestimate the mass and Γ. These simulations do not take into account dark matter halo triaxality, hydrodynamics, star formation or feedback processes.

Campbell et al. (2017) focused on the accuracy of the mass estimators applied to the stellar population of the dwarf galaxies in APOSTLE as a whole. Many of these galaxies, however, turn out to have two (or more) distinct metallicity subpopulations, analogous to those in Sculptor or Fornax. This offers the possibility of testing the validity of the conclusions of Walker & Peñarrubia (2011) using realistic dwarf galaxies formed in state-of-the-art cosmological simulations. This is the goal of this paper. In Section 2 we outline the selection of our simulated galaxy sample and perform an analogous analysis to that of Walker & Peñarrubia (2011). In Section 3, we examine in detail a selection of case studies. We summarize our conclusions in Section 4.

2 SIMULATIONS AND METHODS

2.1 APOSTLE simulations

APOSTLE consists of a suite of zoom-in hydrodynamical simulations of analogues of the Local Group environment (Fattahi et al. 2016; Sawala et al. 2016). The regions were selected for resimulation from the 100 Mpc on a side cosmological *N*-body simulation DOVE (Jenkins 2013). The Milky Way–Andromeda analogues were chosen based on the galaxy pair separations, total mass, relative velocities, recession velocities of the outer Local Group members and consistency with the environment surrounding the Local Group. *WMAP*-7 (*Wilkinson Microwave Anisotropy Probe*) cosmological parameters are assumed: density parameters, $\Omega_{\rm m} = 0.272$, $\Omega_{\rm b} = 0.0455$ and $\Omega_\Lambda = 0.728$; reduced Hubble constant $h = 0.704$; spectral index $n_s = 0.967$ and power spectrum normalization, $\sigma_8 = 0.81$ (Komatsu et al. 2011). An ionizing background is switched on instantaneously at $z = 11.5$.

The regions were resimulated using the EAGLE code, an improved version of the *N*-body/Smooth Particle Hydrodynamics (SPH) code P-GADGET-3 (Springel 2005; Crain et al. 2015; Schaye et al. 2015), including subgrid prescriptions for supernovae and AGN feedback (Booth & Schaye 2009; Dalla Vecchia & Schaye 2012), gas cooling and heating (Wiersma, Schaye & Smith 2009a), reionization, star formation and metal enrichment (Schaye 2004; Schaye & Dalla Vecchia 2008; Wiersma et al. 2009b) and black hole formation and mergers (Rosas-Guevara et al. 2015). The Tree-PM scheme of P-GADGET-3 is used to compute the gravitational acceleration and the ANARCHY SPH scheme (Dalla Vecchia & Schaye 2012; Schaller et al. 2015), based on the pressure-entropy formalism of Hopkins (2013), is used to compute hydrodynamical forces.

Table 1. Dark matter, gas and the ranges of stellar particle masses for the five L1 volumes of APOSTLE used in this work. The gravitational softening at $z = 0$ is 134 pc.

Volume	$m_{\rm DM}{\rm h}^{-1}$ [$\rm M_\odot$]	$m_{\rm gas}{\rm h}^{-1}$ [$\rm M_\odot$]	$m_{\rm star}{\rm h}^{-1}$ [$\rm M_\odot$]
AP-1	3.5×10^4	7.0×10^3	$0.4\text{-}1.4 \times 10^4$
AP-4	1.7×10^4	3.5×10^3	$0.2\text{-}1.0 \times 10^4$
AP-6	3.7×10^4	7.5×10^3	$0.4\text{-}2.5 \times 10^4$
AP-10	3.6×10^4	7.2×10^3	$0.4\text{-}1.2 \times 10^4$
AP-11	3.5×10^4	7.1×10^3	$0.4\text{-}1.6 \times 10^4$

The APOSTLE suite consists of 12 volumes simulated at low and medium resolution (L2 and L3). Five of these were also resimulated at high resolution (L1). In this work we will only consider galaxies within the high-resolution volumes. The gas, dark matter and stellar particle masses for each of these may be found in Table 1.

2.2 Galaxy sample

Haloes in the simulations are identified using the 'friends-of-friends' (FOF) algorithm with linking length of 0.2 times the mean particle separation (Davis et al. 1985). The SUBFIND algorithm is then used to identify gravitationally bound substructures within them (Springel et al. 2001). We define the host and subhalo centres as the centre of their potential (the position of the particle with the most negative potential energy).

Subhaloes bound to the main halo of a group are defined here as 'satellites'; other galaxies in the volume are labelled as 'field' galaxies. When computing the stellar mass of a subhalo, we include all particles located within 0.15 of the virial radius, R_{200}, for field galaxies and particles located within the tidal radius.[1] We limit the sample of satellites and field galaxies to those with a minimum of 1000 stellar particles [corresponding to a stellar mass of the order of $(10^6 - 10^7)\,\rm M_\odot$] to ensure reasonable statistics and good resolution within the half-mass[2] radius. The stellar mass as a function of the maximum circular velocity, $\rm V_{max}$, of galaxies in the five high-resolution volumes is shown in Fig. 1.

In order to identify particles belonging to each stellar subpopulation, for every individual satellite and field galaxy we model the subcomponents using Gaussian Mixture Modelling (GMM) whereby the total metallicity distribution, $p(\log_{10} {\rm Z/Z_\odot})$, is fitted with a combination of two Gaussian probability density functions[3] (Hastie, Tibshirani & Friedman 2001). Five parameters are fit altogether $(w_1, \mu_1, \mu_2, \sigma_1, \sigma_2)$, with w_1 being the relative weight of one of the subpopulations, μ_i the mean metallicity and σ_i the metallicity dispersion. We then assign each particle to a subpopulation if its probability of being in that subpopulation is $p(i) > 0.5$. Effectively, the population is rigidly split at the value of metallicity where the two Gaussians cross. The subpopulation with a higher value of μ_i is denoted as metal-rich and that with the lower μ_i as metal-poor. A sharp cut in metallicity gives rise to some kinematic mixing of the two subpopulations. We have verified that mixing has only a minor

[1] We define the tidal radius of a subhalo as a distance from subhalo centre where the mean enclosed density is equal to that of the host halo up to that distance for satellite galaxies.

[2] We use the term *half-mass radius* to refer to the radius enclosing half the stellar mass as measured directly from the simulations.

[3] As a measure of metallicity we use $\log_{10}{\rm Z/Z_\odot}$, the logarithm of the abundance of elements other than hydrogen and helium. Stellar particles in APOSTLE are spawned probabilistically, with daughter particles inheriting smoothed metal abundances from their parent. For details see Okamoto et al. (2005) and Okamoto, Shimizu & Yoshida (2014).

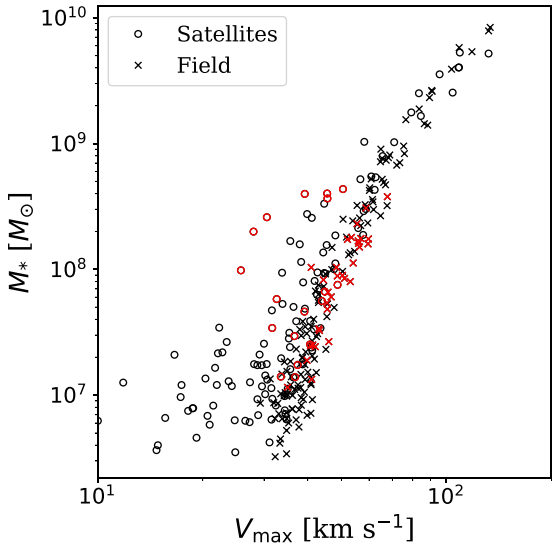

Figure 1. Stellar mass M_* as a function of maximum circular velocity V_{max} for satellite (circles) and field (crosses) galaxies in the five high-resolution volumes of APOSTLE. Galaxies matching the criteria described in Section 2.2 are shown in red. The sample is limited to galaxies with at least 1000 stellar particles to ensure adequate statistics.

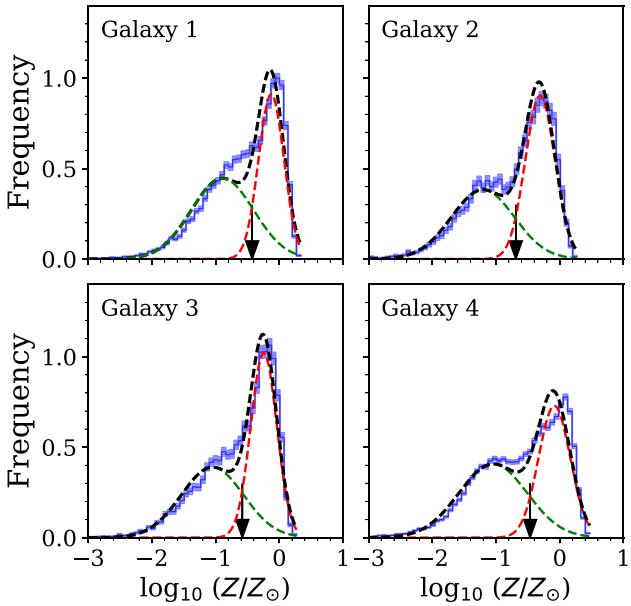

Figure 2. Metallicity histograms of the four galaxies that we use as case studies in this work. The blue curve represents the metallicity distribution and associated Poisson errors. The dashed black line shows the two-Gaussian fit. The dashed red and green lines show the individual Gaussians corresponding to the metal-rich and metal-poor subpopulations, respectively. The arrows show the metallicity at which the population is split. We have assumed a value of the solar metallicity of $Z_\odot = 0.0127$.

effect on the main results of this paper regarding the slope of the halo density profile (see Section A2).

It is important to note, first, that the metallicity distributions of the two subpopulations will not necessarily be Gaussian, but will depend on the specifics of the history of star formation, accretion and mergers. We choose Gaussian probability densities for simplicity. Secondly, cases may exist, where indeed more than two subpopulations are present. These objects would be of great interest for future work due to the possibility of constraining the inner density slope at two or more locations.

In principle, any probability distribution will be better fitted with Gaussian mixtures as the number of fitting parameters is increased. We therefore calculate the Akaike Information Criterion (AIC) corrected for finite sample (Akaike 1998):

$$\mathrm{AIC} = 2k + \chi^2 + \frac{2k(k+1)}{n-k-1}, \quad (5)$$

where k is the number of fitted parameters, n is the number of data points and χ^2 is the chi-squared fit of our model to the data. We take the histogram errors to be Poisson-distributed. The first and third terms in equation (5) represent the penalty on the number of free parameters in the model such that the difference between the AIC values for alternative models is indicative of the information gained by including extra parameters. We find the AIC for a model with a single Gaussian and a model with a mixture of two Gaussians for each galaxy in our sample. We then remove objects where the AIC for a single Gaussian is smaller than that for a mixture of two, as well as those where both models provide a poor fit. A total of 46 per cent of all galaxies satisfy these criteria. The metallicity histograms and subpopulation models of specific objects that we will discuss in particular detail later are shown in Fig. 2.

A simple split into two metallicity subcomponents does not guarantee that they will be spatially segregated. We remove from our sample the objects for which the separation between the two half-light radii is so small as to inflate Γ artificially, as $\Delta \log_{10} r$ approaches zero (see Fig. A1). We therefore discard all objects for which the logarithm of the ratio of 3D half-mass radii $\log_{10}(r_2/r_1) < 0.06$. This condition removes a further 26 per cent of our original sample. For the remaining galaxies, we check that the metal-rich and metal-poor radii are well resolved as judged by the convergence radius defined by Power et al. (2003), at which the collisional relaxation time is approximately equal to the age of the Universe, ensuring that both radii are larger than this value. Overall, of all objects with over 1000 stellar particles in the five high-resolution volumes of APOSTLE, 18 per cent (50 objects) survive our selection criteria. The selected objects are shown in red in Fig. 1; they have stellar masses of the order of 10^7–10^8 M$_\odot$. We find that the fraction of stellar particles assigned to the metal-poor subpopulation ranges between 0.15 and 0.6, consistently with the results of Benítez-Llambay et al. (2016); the metal-rich stellar particles are typically the dominant subcomponent.

2.3 A test of the Walker–Peñarrubia prescription

We now carry out a straightforward test of the accuracy of the logarithmic mass slopes obtained following the Walker & Peñarrubia (2011) prescription. We generate 10 random lines of sight distributed uniformly on the surface of a sphere. For each line of sight, we obtain 1000 bootstrap stellar particle samples for each galaxy, with replacement and, for each sample, we calculate projected half-mass radii, R_e, directly as the projected radius within which half the total stellar mass is contained.[4] We then calculate

[4] According to Gonzalez-Samaniego et al. (2017) this method of estimating R_e results in the bias of ~ 0.9 in the estimated mass seen in the 12 FIRE simulations. However, using a much larger sample of galaxies in APOSTLE, Campbell et al. (2017) found that the mass estimate is, in fact, unbiased. We choose to calculate the projected half-mass radii as in Campbell et al. (2017).

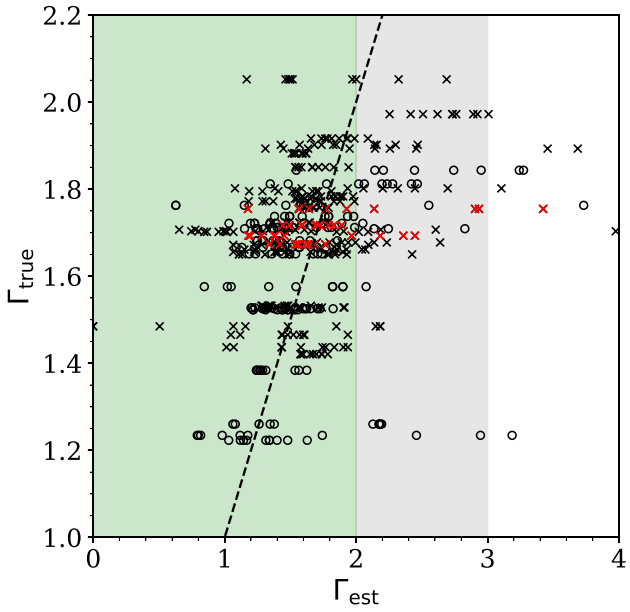

Figure 3. The slope of the logarithmic mass distribution, $\Gamma_{\rm est}$, obtained by applying the Walker et al. (2009) estimator to simulated galaxies in our sample viewed from 10 random directions, plotted against the true slope at the projected 3D half-mass radius, $\Gamma_{\rm true}$. Field galaxies are shown as black crosses and satellites as black circles. Marked in red are the four particular cases that will be further discussed in detail in the next section. The green vertical band shows typical values of $\Gamma_{\rm est}$ for a cusp ($\Gamma = 2$ corresponds to an NFW cusp); the grey band shows values of $\Gamma_{\rm est}$ typical for a core. The dashed line is the one-to-one locus. The slopes obtained from the estimator are slightly underestimated but exhibit significant scatter as the line of sight varies.

the mass-averaged line-of-sight velocity dispersion as:

$$\sigma^2_{\rm LOS} = \frac{\sum (v_i - \bar{v})^2 m_i}{\sum m_i}, \tag{6}$$

where m_i is the mass of each star particle, v_i is the velocity of the particle in projection and $\bar{v}$ is the mean velocity.

Inserting our measured values of $R_{\rm e}$ and $\langle\sigma_{\rm LOS}\rangle$ in the Walker et al. (2009) estimator (equation 2) we obtain the estimated mass within $R_{\rm e}$ of each subpopulation. For each galaxy, we repeat this calculation for the 1000 bootstrap resamplings and for 10 random directions. In Fig. 3 we plot $\Gamma_{\rm true}$, the slope of the line joining the logarithm of the actual mass within the true projected 3D half-mass radius of each subpopulation,[5] as a function of the median values of $\Gamma_{\rm est}$, the slope of the line joining the logarithm of the estimated mass within the measured $R_{\rm e}$ of each subpopulation.

It is clear that the estimated mass slopes tend to be underestimated on average, consistent with findings of Walker & Peñarrubia (2011), and thus the inferred slopes of the density profiles tend to be cuspier than the true values. (Recall that $\Gamma = 2$ corresponds to an NFW cusp, while $\Gamma = 3$ corresponds to a core.) The distribution is asymmetric and exhibits large scatter towards higher values of $\Gamma_{\rm est}$, with some objects reaching $\Gamma_{\rm est} \geq 3$. This bias reflects biases in the measurements of $R_{\rm e}$ and $\langle\sigma_{\rm LOS}\rangle$ as the galaxy is seen from different observer positions. We now investigate why the measured half-mass radii and velocity dispersions vary with the viewing direction.

[5] We take the true projected 3D half-mass radius of an object to be 3/4 of the 3D half-mass radius measured from the simulation.

2.4 Dynamical properties of the simulated galaxies

Campbell et al. (2017) identified asphericity, rotation and velocity anisotropy as the key properties that can introduce uncertainty in mass measurements based on stellar kinematics. We now quantify these properties for *each* metallicity subpopulation within each galaxy in our sample and examine the extent to which the properties of the two subpopulations are correlated with each other.[6]

2.4.1 Sphericity

Here we define the centre of each stellar subpopulation as its centre of mass. The shape of the system is characterized by the reduced inertia tensor (Bett et al. 2007):

$$I_{ij} = \frac{1}{M_{*,\rm sub}} \sum_n m_n \frac{r_{n,i} r_{n,j}}{r_n^2}, \tag{7}$$

where $M_{*,\rm sub}$ is the stellar mass of the subpopulation; m_n is the mass of star particle n; $r_{n,i}$ and $r_{n,j}$ are the coordinates of particle n from the centre of the galaxy in directions i and j. The normalization r_n^2 ensures that only the angular distribution is taken into account, so that the shape is not unduly affected by distant particles. The eigenvectors of the inertia tensor correspond to the axes of the fitted ellipsoid and the eigenvalues, $a^2 \geq b^2 \geq c^2$, to squares of axis lengths. We define the sphericity $s = c/a$; $s = 1$ corresponds to a sphere.

The sphericities of the metal-rich and metal-poor subpopulations in our sample are plotted against each other in the left panel of Fig. 4. The two are positively correlated, albeit with significant scatter caused by one of the subpopulations in certain objects being appreciably more spherical than the other. These cases are of particular interest in this study. Also note that the satellites tend to be less aspherical than the field galaxies. This is likely due to the effects of tidal stripping as discussed in detail in the work of Barber et al. (2015).

2.4.2 Rotation

We quantify the degree to which each subpopulation is supported by rotation by computing $\kappa_{\rm rot}$, the fraction of kinetic energy invested in rotational motion (Sales et al. 2012):

$$\kappa_{\rm rot} = \frac{1}{K_{*,\rm sub}} \sum_n \frac{m_n}{2} \left(\frac{j_{z,n}}{R_{xy,n}}\right)^2, \tag{8}$$

where $K_{*,\rm sub}$ is the stellar kinetic energy of the subpopulation, m_n the mass of star particle n, $j_{z,n}$ the component of the specific angular momentum of the particle in the direction of the total angular momentum and $R_{xy,n}$ the distance of the particle from the angular momentum axis. Objects with $\kappa_{\rm rot} > 0.5$ are considered to be primarily rotation-dominated, while objects with $\kappa_{\rm rot} < 0.5$ are considered to be primarily dispersion-dominated.

The values of $\kappa_{\rm rot}$ for subpopulations of galaxies in our sample are shown in the middle panel of Fig. 4. Our selected objects are

[6] As discussed in Section B1, we have checked that the two subpopulations of the galaxies in our sample have a sufficiently large number of stellar particles for the properties of interest to be numerically converged.

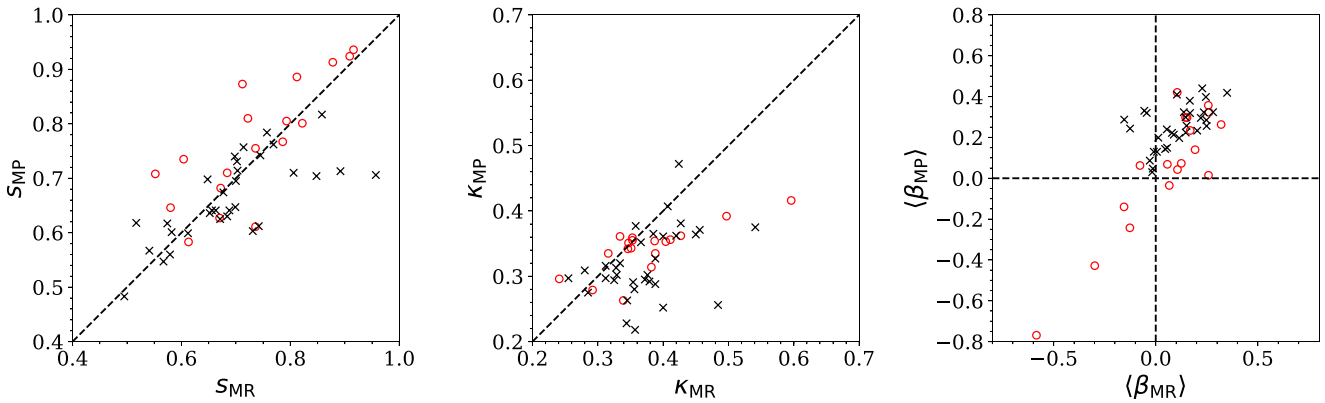

Figure 4. Left: the correlation of the sphericities of the metal-poor and the metal-rich subpopulations for satellites (red circles) and field galaxies (black crosses) in our sample. The dashed line indicates the one-to-one relation. Middle: $\kappa_{\rm rot}$ of the metal-poor and metal-rich subpopulations. Right: The correlation between the average velocity anisotropy of the metal-poor and metal-rich subpopulations. The dashed lines indicate isotropy, $\beta = 0$.

generally dispersion-dominated and a strong bias exists towards higher $\kappa_{\rm rot}$ in the metal-rich subpopulation compared to the metal-poor. All simulated galaxies considered in this work have $\kappa_{\rm rot} < 0.5$ for the galaxy as a *whole*.

2.4.3 *Velocity anisotropy*

The velocity anisotropy is defined as $\beta(r) = 1 - \sigma_{\rm t}^2/2\sigma_{\rm r}^2$, where $\sigma_{\rm r}$ is the radial velocity dispersion and $\sigma_{\rm t}$ the tangential velocity dispersion including the contributions from azimuthal and polar directions. We construct velocity anisotropy profiles by calculating $\sigma_{\rm r}$ and $\sigma_{\rm t}$ for the 32 nearest neighbours of each star particle.

The right panel of Fig. 4 shows the average velocity anisotropy, $\langle\beta\rangle$, for each metallicity subpopulation (the average of local anisotropy of each particle). The majority of the galaxies in our sample tend to have radially biased stellar velocity distributions and the anisotropies are generally correlated in the two metallicity subpopulations. Yet, cases exist where $\langle\beta\rangle$ is radially biased for one subpopulation and tangentially biased or isotropic for the other. As we shall see, such discrepancies affect estimates of Γ.

3 THE EFFECTS OF PROJECTION: FOUR CASE STUDIES

In Fig. 3 we saw that a procedure analogous to that implemented by Walker & Peñarrubia (2011) in their analysis of the kinematics of Sculptor and Fornax dwarfs generally underestimates the logarithmic mass slopes Γ, albeit with a large scatter towards higher values, which would correspond to shallower inner density slopes. We now investigate the factors that affect the accuracy of the procedure. We first examine in detail four illustrative examples and in Section 3.2 we collect the results for our sample of 50 galaxies. We recall that the dark matter density profiles of all the galaxies in our sample are well described by an NFW profile.

The four examples are highlighted in red in Fig. 3. All four are isolated field galaxies, with no recent major mergers. Their two metallicity subpopulations are well segregated spatially. The line-of-sight velocity dispersion of the metal-poor subpopulation is higher than that of the metal-rich subpopulation (see Fig. 5 for the properties of the four examples). In two cases (Galaxies 1 and 2) the procedure on average recovers an accurate value of the slope, but in the other two (Galaxies 3 and 4) the procedure fails and, instead of a cusp, it often returns a profile with a core.

3.1 The effects of misalignment and anisotropy

We view each galaxy from 100 random directions generated uniformly on the surface of a sphere using the spherical spiral method outlined in González (2009). As in Section 2.3, for each line of sight we generate 1000 bootstrap resamplings (with replacement) of the stars in each galaxy and obtain median values of the quantities of interest. In Fig. 6, which is analogous to fig. 10 of Walker & Peñarrubia (2011), we plot the logarithm of the measured projected half-mass radii $R_{\rm e}$ of the bootstrap samples for each viewing angle, along with the corresponding logarithm of masses contained within these radii, inferred using the estimator of equation (2). The measurements are coloured according to the angle between the line of sight and the major axis of the *metal-poor* subpopulation. (The major axes of the two subpopulations will not necessarily be aligned.) The true projected 3D half-mass radius and the enclosed mass of each subpopulation are marked by a cross. The sphericity and value of $\kappa_{\rm rot}$ for each metallicity subpopulation are given in the legend of each panel. For each viewing angle the inferred slope of the cumulative logarithmic mass profile can be obtained by joining points of the same colour in the metal-rich and metal-poor subpopulations. The dashed and dot–dashed lines show the minimum and maximum slopes inferred by this procedure.

The variation with viewing angle of relevant quantities for each galaxy is plotted in Fig. 7 and is discussed below. In this plot, α denotes the ratio, $M_{\rm est}/M_{\rm true}$, of the estimated to the true mass, where the true mass includes the dark matter, stellar and gas particles within the projected 3D half-mass radius; λ is the ratio, $\Gamma_{\rm est}/\Gamma_{\rm true}$, of the estimated to the true slope of the cumulative logarithmic mass profile, where $\Gamma_{\rm est}$ is the slope measured between the measured values of $R_{\rm e}$ and $\Gamma_{\rm true}$ is the slope between the projected true 3D half-mass radii of the two subpopulations.

Apart from the metal-rich subpopulation of Galaxy 4, which is close to spherical, all other subpopulations in the four examples of Fig. 6 are quite elongated. For the nearly spherical subpopulation, the estimated projected half-mass radius is, not surprisingly, almost independent of viewing angle. The values of the estimated mass show a mild systematic dependence on viewing angle which reflects the weak dependence of the velocity dispersion on the line of sight seen in Fig. 7.

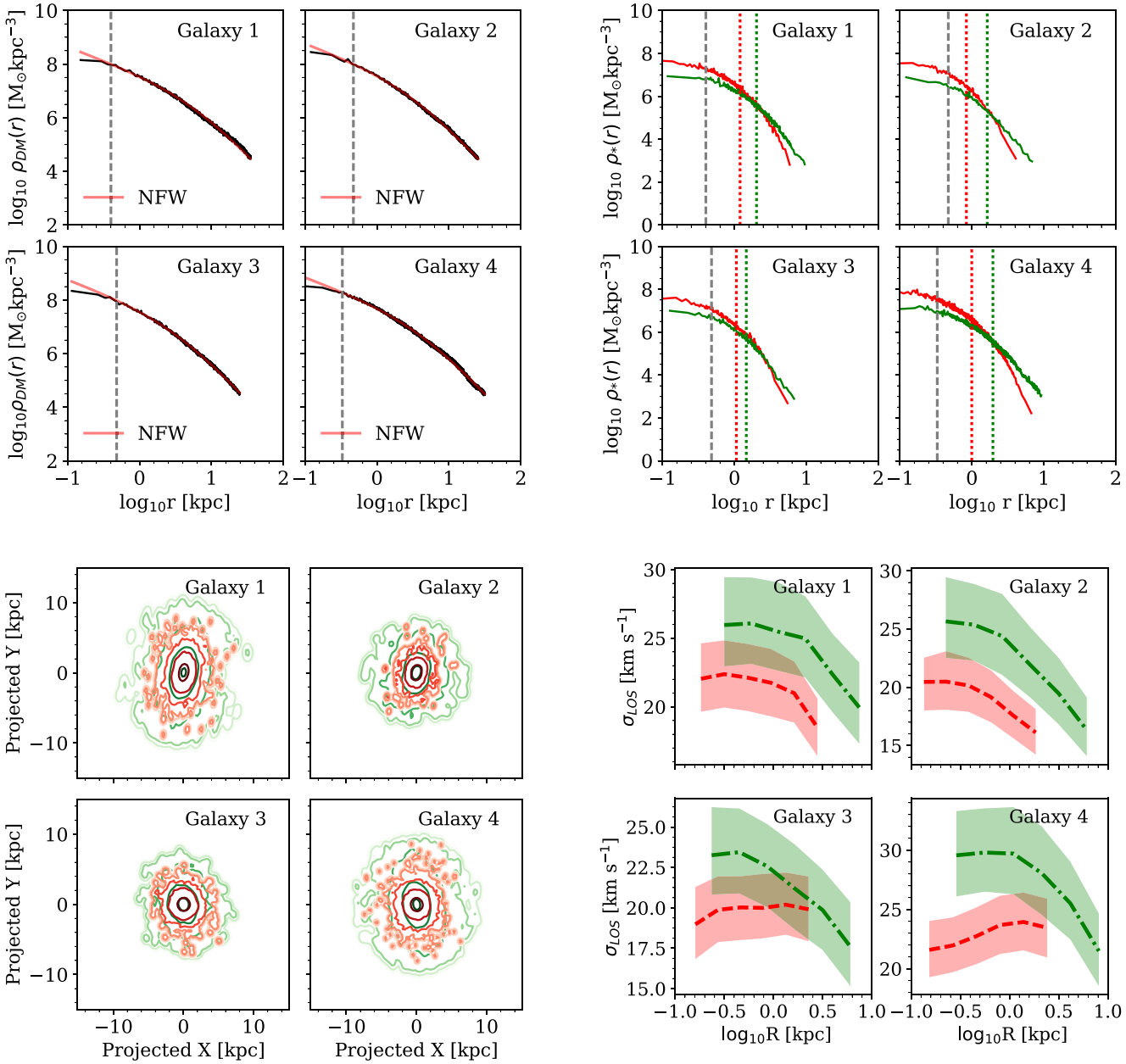

Figure 5. Upper left: dark matter profiles for the four illustrative examples discussed in this section. As for all galaxies in our sample, the inner density slope has a cusp; the best-fitting NFW profile is shown in red. The grey dashed line marks the convergence radius defined by Power et al. (2003). Upper right: stellar density profiles for the metal-rich (red) and metal-poor subpopulations (green) for the four examples. The grey dashed line marks the convergence radius and the red and green dotted lines show the 3D half-mass radii of the metal-rich and metal-poor subpopulations, respectively. The metal-poor component is more extended, with the metal-rich population concentrated near the centre. Lower left: probability density contours of the spatial distribution of stars in the four galaxies. The red and green contours represent the metal-rich and metal-poor subpopulations, respectively, with the highest contour enclosing $p(x,)y = 0.1$ and lower ones decreasing in probability density by factors of 10. The galaxies are viewed along the direction of the intermediate axis of the metal-poor subpopulation. Lower right: velocity dispersion profiles for the four examples, projected over 100 lines of sight, as a function of projected distance from the centre. The red dashed line and the green dash–dotted line show the medians of the metal-rich and the metal-poor subpopulations, respectively. The bands show the 1σ scatter. The metal-rich subpopulation is kinematically colder than the metal-poor subpopulation at small radii.

The situation is quite different for the elongated subpopulations. Let us consider, for example, the metal-poor subpopulation of Galaxy 4. Its sphericity is $s_{\rm MP} = 0.71$, quite typical for our sample (see Fig. 4). Now the measured values of the projected half-mass radius vary greatly with viewing angle, from 1.2 kpc when the subpopulation is viewed along its major axis to 1.6 kpc when it is viewed along the perpendicular direction. Since the velocity anisotropy is radially biased (see Fig. 4), the measured velocity dispersion varies with viewing angle, from 33 km s^{-1} when viewed along the major axis to 27 km s^{-1} when viewed along the perpendicular direction. This decrease in velocity dispersion largely balances the increase in the projected half-mass radius with the result that the estimated mass of the metal-poor population varies little with viewing angle, by only $\sim$0.1 dex. Thus, a very similar mass is

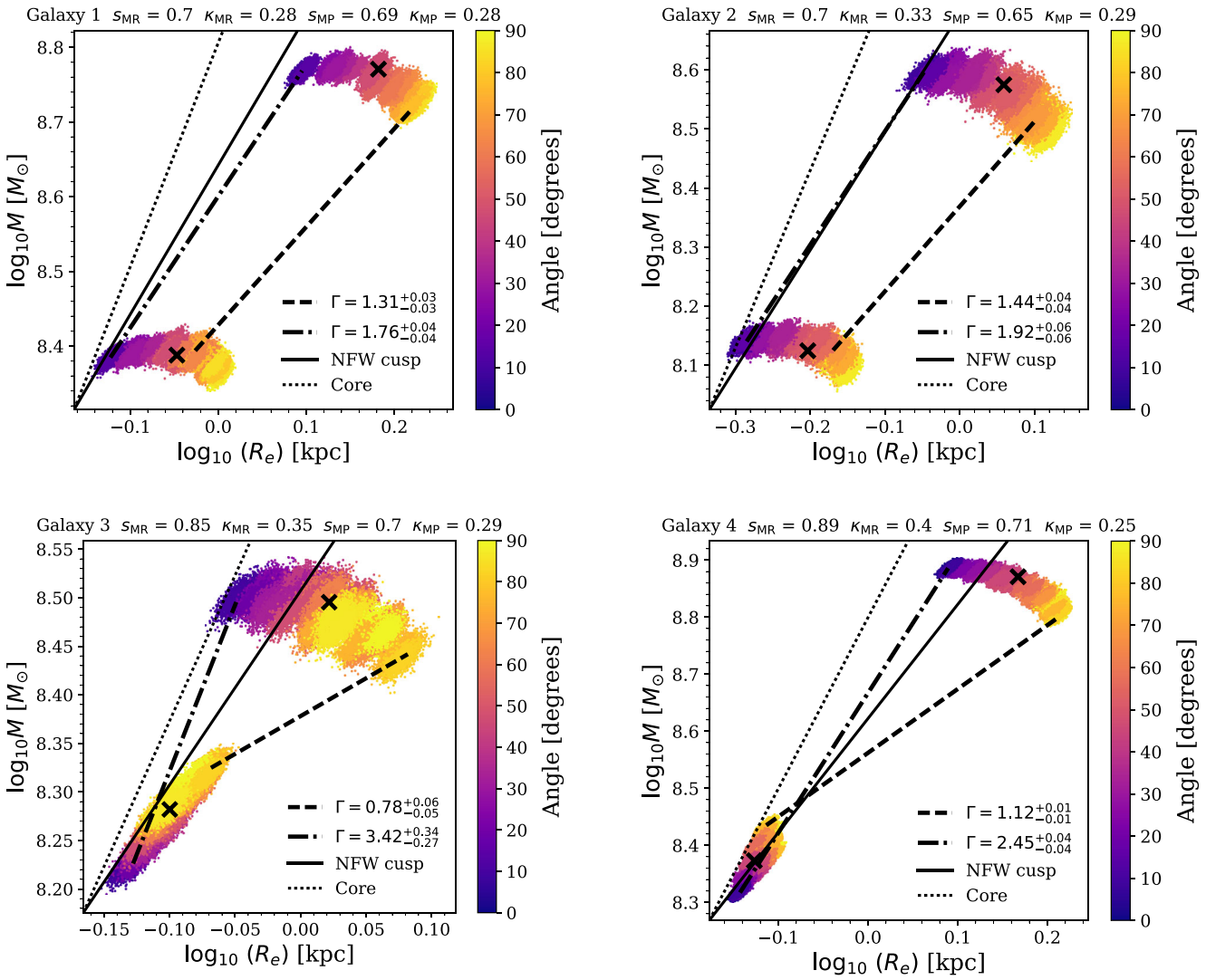

Figure 6. Logarithmic mass slopes for our four illustrative examples. The dots show measured projected half-mass radii and associated contained mass inferred from the Walker et al. (2009) estimator of equation (2) for each of the 1000 bootstrap resamplings of each galaxy; each galaxy is seen from 100 different directions. The points are coloured according to the viewing angle measured from the major axis of the metal-poor subpopulation. The black dashed and dash–dotted lines show the minimum and maximum slopes obtained from all 100 lines of sight, respectively. For reference, the black solid and dotted lines show the slopes of an NFW cusp and a core. The black crosses denote the true projected 3D half-mass radii and the masses within them, taken directly from the simulation. The labels above each panel give the sphericity and value of $\kappa_{\rm rot}$ for each subpopulation. A large scatter in projected half-mass radius can be seen in subpopulations that are strongly aspherical ($s < 1$).

associated with a relatively large range of projected half-mass radii. The biases in the measured mass are anticorrelated as the viewing angle varies, as shown in the third row of Fig. 7.

As Figs 6 and 7 show, the result is that the inferred slope of the cumulative logarithmic mass profile for Galaxy 4 can take on a wide range of values, from $\Gamma = 2.45$ when the galaxy is viewed along the major axis of the metal-poor population to $\Gamma = 1.12$ when it is viewed along the perpendicular direction. Thus, for viewing angles between about 0 and 50°, the mass distribution in this galaxy would, incorrectly, be measured to have a core.

Galaxies 1 and 2 are also quite elongated. However, in these two cases, both subpopulations are aspherical and their major axes are roughly aligned. Now the behaviour we have just seen for the metal-poor subpopulation of Galaxy 4 is reproduced *for both subpopulations*. The result is that both the projected half-mass radius and the mass contained within it for both subpopulations are incorrectly estimated by roughly the same factors and these biases vary similarly with viewing angle (third row of Fig. 7). Thus, although the masses and radii of both subpopulations are incorrectly estimated, the slopes come out roughly right: these two galaxies are correctly inferred to have cusps.

Galaxy 3 is an intermediate case. Its metal-poor subpopulation has similar sphericity to the metal-poor subpopulation of Galaxy 4 so the measured projected half-mass radius varies by a similar factor. While the inferred mass has greater scatter at a given viewing angle, the overall variation is still only slightly larger than 0.1 dex. The half-mass radius of the metal-rich subpopulation of Galaxy 3 shows some dependence on viewing angle (see Fig. 7). In this case, the systematic variation of the inferred mass is larger and, as seen in Fig. 7, it increases with viewing angle. This is enough to

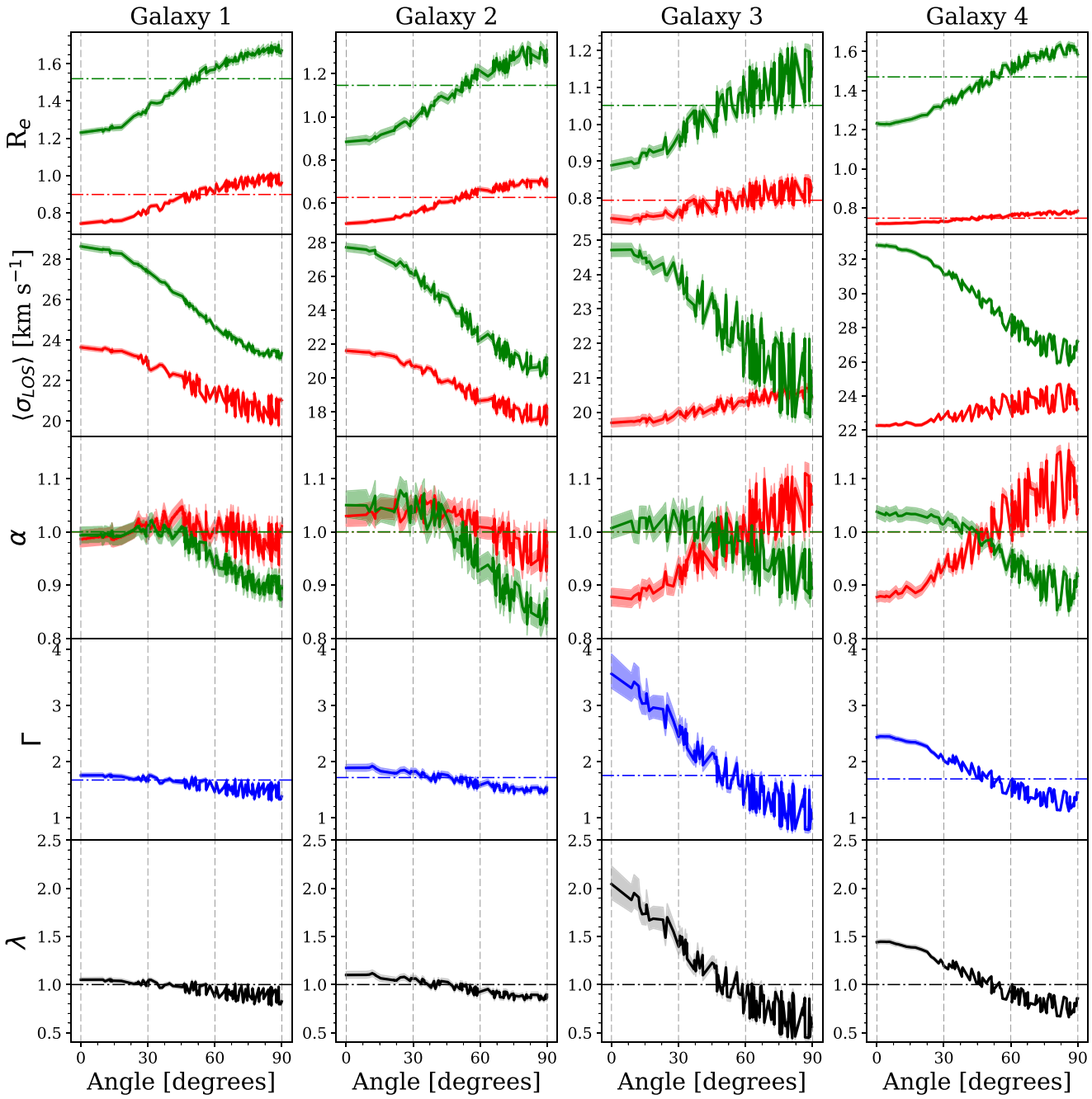

Figure 7. The variation with viewing angle of some of the key properties of our four illustrative example galaxies. Angle is the viewing angle measured from the major axis of the metal-poor subpopulation. Red and green colours represent the metal-rich and metal-poor subpopulations, respectively. First row: the projected half-mass radius measured for each subpopulation. Second row: the estimated mass-weighted average line-of-sight velocity dispersion. For Galaxies 3 and 4 the velocity dispersion of the metal-rich subpopulation is anticorrelated with that of the metal-poor subpopulation. Third row: the accuracy of the mass estimator for each subpopulation, $\alpha = M_{\rm est}/M_{\rm true}$. Fourth row: the measured slope of the cumulative logarithmic mass distribution, Γ. Fifth row: the accuracy of the measured mass slope, $\lambda = \Gamma_{\rm est}/\Gamma_{\rm true}$.

result in a wide range of estimated slopes. Similarly to Galaxy 4, this galaxy would be measured to have a core for viewing angles between about 20° and 50° and for even smaller viewing angles it would be measured to have a 'hole' in the central region ($\Gamma > 3$).

Although the systematic errors in the estimates of the slope of the cumulative logarithmic mass distribution using a procedure analogous to that of Walker & Peñarrubia (2011) result from a complex interplay between projection and kinematic effects, it is clear that a major factor behind them is the significant elongation of the stellar subpopulations, and particularly the misalignment between the major axes of the metal-rich and metal-poor subpopulations seen in a number of cases, including Galaxy 4. This lack of similarity arises naturally in our simulations and is linked to the different formation paths of the two subpopulations (Benítez-Llambay et al. 2016), which we will investigate in a subsequent paper.

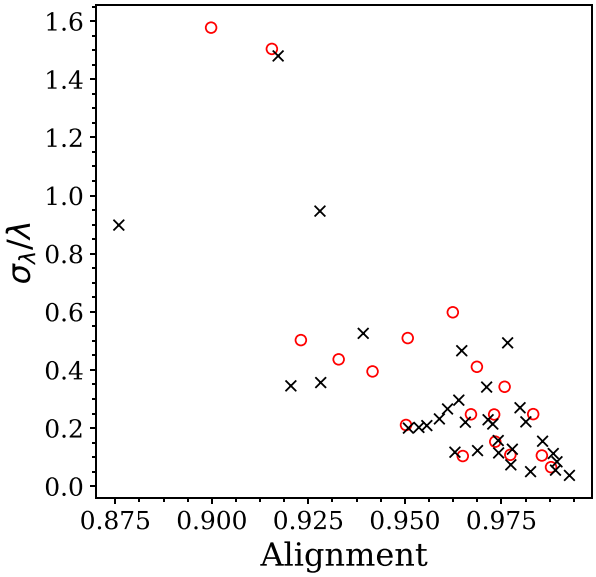

Figure 8. Relative upper error (the difference between the 84$^{\rm th}$ and the 50$^{\rm th}$ percentile divided by the median value) on the mass slope accuracy, λ, as a function of the alignment of the metal-rich and the metal-poor subpopulations, as defined in Section 3.1. Satellites and field galaxies are shown with red circles and black crosses, respectively. Measurements in galaxies with more misaligned subpopulations are more likely to return larger values of Γ.

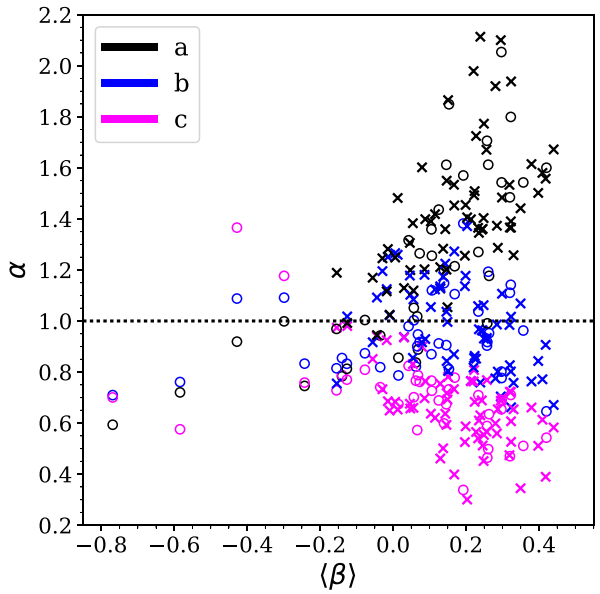

Figure 9. The accuracy of the mass estimator, $\alpha = M_{\rm est}/M_{\rm true}$, for the metal-rich and metal-poor subpopulations of all galaxies in our sample, as a function of the average velocity anisotropy, $\langle\beta\rangle$. The galaxies are viewed along their major (black), intermediate (blue) and minor (magenta) axes of each subpopulation. The black dotted line shows accurate mass estimates ($\alpha = 1$). Satellite galaxies are shown as circles and field galaxies as crosses. Along the major axis, the masses tend to be overestimated for subpopulations with radial anisotropy. For nearly isotropic subpopulations the accuracy is similar for all three directions.

In order to quantify the effect of both the misalignment of the principal axes and the differences in sphericity of the two subpopulations on the scatter in the estimated logarithmic mass slopes, we define the following alignment statistic. We model the two subpopulations as concentric ellipsoids of unit volume, with axis ratios equal to those measured for each subpopulation and an offset angle equal the angle between the major axes of the two subpopulations. We then compute the fraction of volume within the intersection of the two ellipsoids. Subpopulations with similar axis ratios and spatial orientation would therefore have an alignment close to 1. In Fig. 8 we show the relative upper error (the difference between the 84$^{\rm th}$ and 50$^{\rm th}$ percentiles divided by the median value) on the slope accuracy, λ, as a function of the value of the alignment statistic. It is clear that measurements for galaxies with more misaligned subpopulations tend to return higher values of Γ, corresponding to shallower inner density slopes.

The non-trivial radial variation of the velocity anisotropy, β, which is generally different for the two metallicity subpopulations (see Fig. 4), also plays a role. This can be seen in Fig. 9, where we plot α, the error in the estimate of the mass for each of the two subpopulations in our sample, as a function of the average anisotropy parameter $\langle\beta\rangle$, when each subpopulation is viewed from directions aligned with the three principal axes. For directions along the minor and intermediate axes the values of α scatter about $\alpha = 1$, although there is a bias towards $\alpha < 1$, that is for an underestimate of the mass when the subpopulation is viewed along its minor axis. However, when the subpopulation is viewed along its major axis and the velocity anisotropy has a radial bias ($\beta > 0$), its mass tends to be *overestimated* [in agreement with the conclusions of Kowalczyk et al. (2013)] and the size of this bias increases systematically with increasing anisotropy. Along this particular viewing angle the velocity dispersion is generally largest. When the velocity distribution is isotropic or tangentially biased, however, the mass is correctly estimated. (This is the reason why the estimate of the mass of the metal-rich subpopulation of Galaxy 3, which has an isotropic velocity distribution, is unbiased.)

3.2 Accuracy of the inferred mass slope for the sample as a whole

In this subsection we present statistical results for our sample of 50 galaxies. This sample was selected according to the specific criteria described in Section 2.2, essentially requiring that there be two well-separated metallicity subpopulations, as judged by the statistic introduced in that section. These criteria need not match in detail those used for real objects. At present there are only a handful of two-metallicity subpopulation galaxies known and those populations have been identified somewhat serendipitously. Nevertheless, our statistical results should be indicative of the frequency with which we might expect the slope of the dark matter density profile to be incorrectly estimated.

The top panel of Fig. 10 shows the distributions of $\Gamma_{\rm est}$ and $\lambda = \Gamma_{\rm est}/\Gamma_{\rm true}$ for the 1000 bootstrap resamplings of each galaxy in our sample, each viewed from 100 different random directions. (Recall that an NFW profile has $\Gamma = 2$ as $r \to 0$ and a profile with a constant-density core has $\Gamma = 3$.) The distribution of $\Gamma_{\rm est}$ is asymmetric with mean value $\Gamma = 1.59^{+0.46}_{-0.37}$ and $\lambda = 0.95^{+0.28}_{-0.19}$ for the Walker et al. (2009) estimator, implying that Γ is underestimated on average by ~ 5 per cent; the true value (corresponding to $\lambda = 1$) lies within 1σ of the mean. Slopes tend to be overestimated by $\sim$3 per cent on average using the Wolf et al. (2010) estimator, with $\lambda = 1.03^{+0.29}_{-0.21}$.

Flatter slopes than NFW, $\Gamma > 2$ are measured in $\sim$17.8 per cent of cases and $\Gamma > 3$ (corresponding to a 'hole' in the centre) in

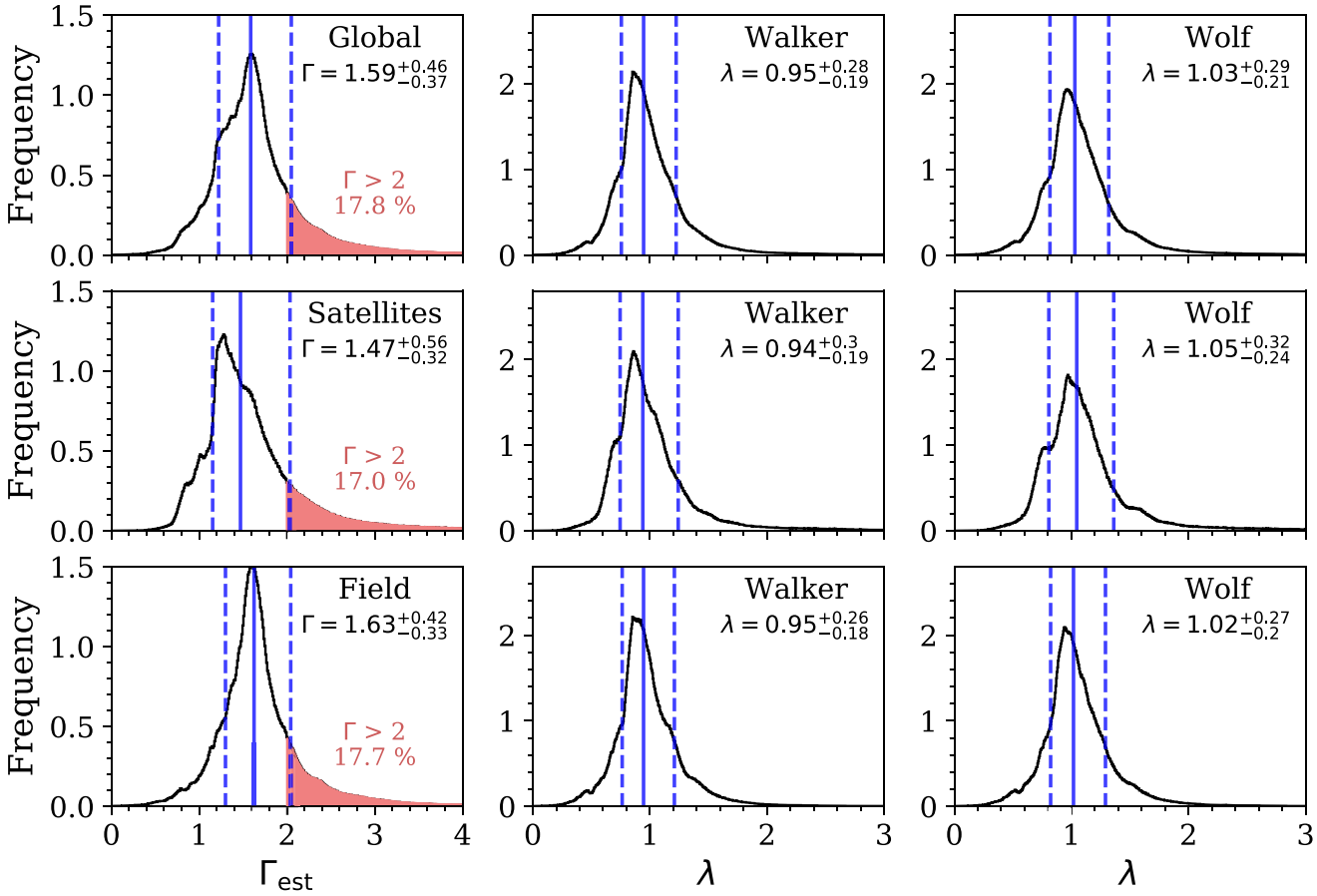

Figure 10. Top panel: overall distributions for the 50 objects in our sample of the measured slope, $\Gamma_{\rm est}$ (left), and slope accuracy, $\lambda = \Gamma_{\rm est}/\Gamma_{\rm true}$, for (middle) the Walker et al. (2009) estimator and (right) the Wolf et al. (2010) estimator. Blue solid lines show the median values and the blue dashed lines show 16$^{\rm th}$ and 84$^{\rm th}$ percentiles. The slopes tend to be underestimated by 5 per cent on average using the Walker et al. (2009) estimator and overestimated by 3 per cent on average using the Wolf et al. (2010) estimator; the distribution of λ is not symmetrical. $\Gamma \geq 2$ is measured in 17.8 per cent of cases and $\Gamma \geq 3$ in ∼3.5 per cent of cases. Middle panel: same as above, but only for the 18 satellite galaxies in our sample. Bottom panel: as above, but showing the distributions of Γ and λ only for the 32 field galaxies in our sample. The estimators perform in a similar way for both satellites and field galaxies.

∼3.5 per cent of cases. In the middle and bottom panels we show equivalent distributions for satellite and field galaxies in our sample. Whilst the satellites generally tend to exhibit cuspier inner slopes ($\Gamma_{\rm est} = 1.47^{+0.56}_{-0.32}$ compared to $\Gamma_{\rm est} = 1.63^{+0.42}_{-0.33}$ for field dwarfs), the distribution of the accuracy of the inferred slopes, λ, is similar to that of the field galaxies. The greater scatter towards higher values of Γ in satellites can be explained by the fact that a greater fraction of satellites than field galaxies in our sample exhibit strong misalignment, as shown in Fig. 8. We have additionally verified that if we identify the true slope with the slope of the line joining the logarithm of true masses within $R_{\rm e}$ of each subpopulation, the bias and scatter in λ remain unaffected.

Walker & Peñarrubia (2011), who used the Walker et al. (2009) estimator, found $\Gamma = 2.95^{+0.51}_{-0.39}$ for Sculptor and $\Gamma = 2.61^{+0.43}_{-0.37}$ for Fornax and concluded that these values exclude the NFW profile with significance greater than 99 and 96 per cent, respectively. However, according to the distribution of $\Gamma_{\rm est}$ in Fig. 10 for the Walker et al. (2009) and Wolf et al. (2010) estimators derived from our simulations, these values of Γ are only inconsistent with the NFW profile at 93.6 and 88.9 significance for Sculptor and Fornax, respectively (where we have taken the 1σ lower limit of the original estimates).

4 DISCUSSION AND CONCLUSIONS

The question of whether or not the dark matter haloes of galaxies have central, constant-density cores is of great interest in cosmology. It is now well established that, in the absence of baryon effects, haloes of all masses develop NFW profiles (Navarro et al. 1996, 1997) which have a central cusp. An incontrovertible measurement of a core would therefore have important implications: it would either signal the impact of exotic baryonic effects (Navarro et al. 1996; Pontzen & Governato 2012) or of exotic types of particles such as self-interacting dark matter (Spergel & Steinhardt 2000). Unfortunately, measuring dark matter profiles in the innermost regions of haloes, encompassing only at most a few per cent of the halo mass, is difficult.

In this work we have tested the Walker & Peñarrubia (2011) procedure for inferring the slope of the inner dark matter halo profile in galaxies with two metallicity subpopulations using galaxies from the APOSTLE cosmological simulations. These follow not only the evolution of dark matter, but also the evolution of gas, and incorporate subgrid prescriptions to model the processes thought to be at play in galaxy formation. The initial conditions correspond to a cold dark matter universe but are conditioned to form an analogue of the Local Group at the final time. Thus, this is the first test of the

Walker & Peñarrubia (2011) procedure in fully realistic simulations which produce dwarf galaxies *ab initio*. These are not guaranteed to satisfy the key assumptions underlying the Wolf et al. (2010) and Walker et al. (2009) mass estimators: sphericity and dynamical equilibrium, and, indeed, many of our simulated galaxies violate them to varying degrees.

Gratifyingly, our simulations produce dwarf galaxies with two identifiable metallicity subpopulations reminiscent of Sculptor and Fornax. Out of 286 model galaxies resolved with more than 1000 stellar particles we identify 50 dwarfs with dual metallicity subpopulations, according to the criteria discussed in Section 2.2. Their kinematical properties are summarized in Fig. 4. The subpopulations tend to be significantly aspherical and often develop different asphericities: ∼30 per cent of galaxies in our sample have metal-rich and metal-poor subpopulations differing in sphericity by over 10 per cent and, in many cases, the orientation of their major axes differs as well. The metal-rich subpopulations tend to show more rotation than the metal-poor ones and the velocity anisotropy of the subpopulations can also differ substantially. These differences occur both in satellites and in field dwarfs. The lack of similarity arises naturally in our simulations and is linked to the different formation paths of the two subpopulations (which we will investigate in a subsequent paper).

Our main result is that the method introduced by Battaglia et al. (2008) and extended by Walker & Peñarrubia (2011), based on comparing the masses interior to the half-mass radii of the metal-rich and metal-poor subpopulations, can often lead to an incorrect inference of the slope of the inner profile of the galaxies' dark matter haloes. All the haloes in our simulations have cuspy NFW profiles, yet 17.8 per cent of the galaxies in our sample would be inferred to have flatter, core-like profiles. Multiple factors play a role in these failures but the main culprit is misalignment of the two elongated metallicity subpopulations (which generally have radially varying velocity anisotropy). This results in a wide range of inferred slopes for the mass distribution depending on the viewing angle. Four specific examples illustrating cases when the slope is correctly or incorrectly inferred have been shown.

The study of Walker & Peñarrubia (2011) is sometimes regarded as one of the more convincing arguments for the presence of cores in the dark matter haloes of dwarf galaxies (Amorisco & Evans 2012). However, their proposed method of measuring cumulative logarithmic mass profile slopes relies heavily on the assumption that the properties of the two metallicity subpopulations are correlated, such that any bias in the application of the mass estimator would cancel when obtaining the slope. This assumption fails in a number of our simulated galaxies where not only the elongation and orientation, but also the orbital anisotropy differs for the two subpopulations. Of course it remains to be seen whether the properties of the two metallicity subpopulations in Sculptor and Fornax are correlated or not, but this is not currently feasible. The availability of proper motion data for individual stars within these galaxies would allow us to somewhat take away the dependence of the accuracy of the mass estimator on the angle of view, although, for an instrument like *Gaia*, the measurement uncertainties for a galaxy as distant as Sculptor is expected to be comparable to the velocities themselves (Jin, Helmi & Breddels 2015; Gaia Collaboration et al. 2016). Given the sensitivity of the inferred slope to the viewing angle that we have demonstrated in this work, we concur with Kowalczyk et al. (2013) that a large statistical sample of *randomly oriented* galaxies is highly desirable. But for any particular observation, knowledge of the sphericity and velocity anisotropy of both subpopulations and their orientation with respect to one another and to the observer is required before any definitive conclusion can be reached regarding the slope of the galaxy's inner dark matter halo.

ACKNOWLEDGEMENTS

We thank the anonymous referee for useful comments that helped us improve the final version of this work. We are also grateful for helpful discussions with Marius Cautun, Aaron Ludlow, Matthieu Schaller, Louis Strigari and Alis Deason. This work was supported by the Science and Technology Facilities Council grants ST/L00075X/1 and ST/P000451/1. AG acknowledges an STFC studentship funded by STFC grant ST/N50404X/1. This work used the DiRAC Data Centric system at Durham University, operated by the Institute for Computational Cosmology on behalf of the STFC DiRAC HPC Facility (www.dirac.ac.uk). This equipment was funded by BIS National E-infrastructure capital grant ST/K00042X/1, STFC capital grant ST/H008519/1, STFC DiRAC Operations grant ST/K003267/1 and Durham University. DiRAC is part of the National E-Infrastructure. This work has also benefited from the use of NUMPY and SCIPY.

REFERENCES

Adams J. J. et al., 2014, ApJ, 789, 63
Agnello A., Evans N. W., 2012, ApJ, 754, L39
Akaike H., 1998, Information Theory and an Extension of the Maximum Likelihood Principle. Springer-Verlag, New York, p. 199
Amorisco N. C., Evans N. W., 2012, MNRAS, 419, 184
Barber C., Starkenburg E., Navarro J. F., McConnachie A. W., 2015, MNRAS, 447, 1112
Battaglia G. et al., 2006, A&A, 459, 423
Battaglia G., Helmi A., Tolstoy E., Irwin M., Hill V., Jablonka P., 2008, ApJ, 681, L13
Battaglia G., Tolstoy E., Helmi A., Irwin M., Parisi P., Hill V., Jablonka P., 2011, MNRAS, 411, 1013
Benítez-Llambay A., Navarro J. F., Abadi M. G., Gottlöber S., Yepes G., Hoffman Y., Steinmetz M., 2016, MNRAS, 456, 1185
Bett P., Eke V., Frenk C. S., Jenkins A., Helly J., Navarro J., 2007, MNRAS, 376, 215
Booth C. M., Schaye J., 2009, MNRAS, 398, 53
Breddels M. A., Helmi A., van den Bosch R. C. E., van de Ven G., Battaglia G., 2013, MNRAS, 433, 3173
Brooks A. M., Zolotov A., 2014, ApJ, 786, 87
Campbell D. J. R. et al., 2017, MNRAS, 469, 2335
Cole D. R., Dehnen W., Wilkinson M. I., 2011, MNRAS, 416, 1118
Crain R. A. et al., 2015, MNRAS, 450, 1937
Dalla Vecchia C., Schaye J., 2012, MNRAS, 426, 140
Davis M., Efstathiou G., Frenk C. S., White S. D. M., 1985, ApJ, 292, 371
Del Popolo A., Kroupa P., 2009, A&A, 502, 733
El-Zant A., Shlosman I., Hoffman Y., 2001, ApJ, 560, 636
Fattahi A. et al., 2016, MNRAS, 457, 844
Flores R. A., Primack J. R., 1994, ApJ, 427, L1
Gaia Collaboration et al., 2016, A&A, 595, A1
Gilmore G., Wilkinson M. I., Wyse R. F. G., Kleyna J. T., Koch A., Evans N. W., Grebel E. K., 2007, ApJ, 663, 948
González Á., 2009, Math. Geosci., 42, 49
Gonzalez-Samaniego A., Bullock J. S., Boylan-Kolchin M., Fitts A., Elbert O. D., Hopkins P. F., Kereš D., Faucher-Giguère C.-A., 2017, MNRAS, 472, 4786
Hastie T., Tibshirani R., Friedman J., 2001, The Elements of Statistical Learning. Springer Series in Statistics. Springer New York Inc., New York
Hopkins P. F., 2013, MNRAS, 428, 2840
Jenkins A., 2013, MNRAS, 434, 2094
Jin S., Helmi A., Breddels M., 2015, preprint (arXiv:1502.01215)

Kawata D., Arimoto N., Cen R., Gibson B. K., 2006, ApJ, 641, 785
Komatsu E. et al., 2011, ApJS, 192, 18
Kowalczyk K., Łokas E. L., Kazantzidis S., Mayer L., 2013, MNRAS, 431, 2796
Kuzio de Naray R., McGaugh S. S., de Blok W. J. G., Bosma A., 2006, ApJS, 165, 461
Laporte C. F. P., Walker M. G., Peñarrubia J., 2013a, MNRAS, 433, L54
Laporte C. F. P., White S. D. M., Naab T., Gao L., 2013b, MNRAS, 435, 901
Mashchenko S., Wadsley J., Couchman H. M. P., 2008, Science, 319, 174
Moore B., 1994, Nature, 370, 629
Navarro J. F., Eke V. R., Frenk C. S., 1996, MNRAS, 283, L72
Navarro J. F., Frenk C. S., White S. D. M., 1997, ApJ, 490, 493
Oh S. H., Brook C., Governato F., Brinks E., Mayer L., de Blok W. J. G., Brooks A., Walter F., 2011, AJ, 142, 24
Oh S. H. et al., 2015, AJ, 149, 180
Okamoto T., Eke V. R., Frenk C. S., Jenkins A., 2005, MNRAS, 363, 1299
Okamoto T., Shimizu I., Yoshida N., 2014, PASJ, 66, 70
Oman K. A., Marasco A., Navarro J. F., Frenk C. S., Schaye J., Benítez-Llambay A., 2017, MNRAS, preprint (arXiv:1706.07478)
Pineda J. C. B., Hayward C. C., Springel V., Mendes de Oliveira C., 2017, MNRAS, 466, 63
Pontzen A., Governato F., 2012, MNRAS, 421, 3464
Power C., Navarro J. F., Jenkins A., Frenk C. S., White S. D. M., Springel V., Stadel J., Quinn T., 2003, MNRAS, 338, 14
Pryor C., Kormendy J., 1990, AJ, 100, 127
Read J. I., Gilmore G., 2005, MNRAS, 356, 107
Richardson T., Fairbairn M., 2014, MNRAS, 441, 1584
Rosas-Guevara Y. M. et al., 2015, MNRAS, 454, 1038
Sales L. V., Navarro J. F., Theuns T., Schaye J., White S. D. M., Frenk C. S., Crain R. A., Dalla Vecchia C., 2012, MNRAS, 423, 1544
Sánchez-Salcedo F. J., Reyes-Iturbide J., Hernandez X., 2006, MNRAS, 370, 1829
Sawala T. et al., 2016, MNRAS, 457, 1931
Schaller M., Dalla Vecchia C., Schaye J., Bower R. G., Theuns T., Crain R. A., Furlong M., McCarthy I. G., 2015, MNRAS, 454, 2277
Schaye J., 2004, ApJ, 609, 667
Schaye J., Dalla Vecchia C., 2008, MNRAS, 383, 1210
Schaye J. et al., 2015, MNRAS, 446, 521
Spergel D. N., Steinhardt P. J., 2000, Phys. Rev. Lett., 84, 3760
Springel V., 2005, MNRAS, 364, 1105
Springel V., White S. D. M., Tormen G., Kauffmann G., 2001, MNRAS, 328, 726
Springel V. et al., 2008, MNRAS, 391, 1685
Strigari L. E., Frenk C. S., White S. D. M., 2010, MNRAS, 408, 2364
Strigari L. E., Frenk C. S., White S. D. M., 2014, AAS, preprint (arXiv:1406.6079)
Tolstoy E. et al., 2004, ApJ, 617, L119
Walker M. G., Peñarrubia J., 2011, ApJ, 742, 20
Walker M. G., Mateo M., Olszewski E. W., Peñarrubia J., Wyn Evans N., Gilmore G., 2009, ApJ, 704, 1274
Weinberg M. D., Katz N., 2002, ApJ, 580, 627
Wiersma R. P. C., Schaye J., Smith B. D., 2009a, MNRAS, 393, 99
Wiersma R. P. C., Schaye J., Theuns T., Dalla Vecchia C., Tornatore L., 2009b, MNRAS, 399, 574
Wolf J., Martinez G. D., Bullock J. S., Kaplinghat M., Geha M., Muñoz R. R., Simon J. D., Avedo F. F., 2010, MNRAS, 406, 1220

APPENDIX A

A1 Definition of Γ

By definition, the value of Γ becomes undefined as the radii of the two metallicity subpopulations coincide, $\Delta \log_{10} r_2/r_1 \rightarrow 0$. In selecting our sample, it is therefore important to include only galaxies in which the two subpopulations are well separated. We applied the GMM technique to all galaxies in the five high-resolution

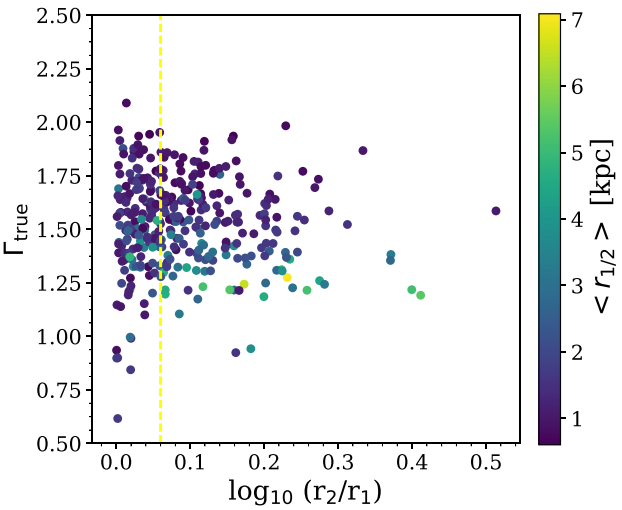

Figure A1. True slope of the cumulative mass function as a function of the ratio of the half-mass radius of the metal-poor and the metal-rich subpopulations. The points are coloured by the mean of the metal-poor and the metal-rich half-mass radii. $\Gamma_{\rm true}$ reaches low values below $\log_{10}(r_2/r_1) \sim 0.06$ as a near-zero value of $\Delta \log_{10} {\rm M}$ becomes comparable to near zero values of $\Delta \log_{10} {\rm r}$. At much larger separations the slope is measured further away from the centre and is correspondingly steeper.

APOSTLE simulations and, for each, we measured the 3D half-mass radius of the metal-rich and the metal-poor subpopulations and obtained the slope $\Gamma_{\rm true}$. Fig. A1 shows $\Gamma_{\rm true}$ as a function of the ratio of the 3D half-mass radii of the two metallicity subpopulations. Below $\log_{10}(r_2/r_1) \sim 0.06$, where r_2 is the larger radius of the two, very low values of $\Gamma_{\rm true}$ are obtained. We require $\log_{10}(r_2/r_1) > 0.06$ for our sample, as shown by the dashed yellow line in Fig. A1.

A2 Subpopulation mixing

As described in Section 2.2, we define each subpopulation by placing a rigid cut at the intersection of two fitted Gaussians. This treatment ignores mixing between the two subpopulations, which can affect the measurement of the velocity dispersion, thus introducing a correlation in the kinematics of the metal-rich and the metal-poor subpopulations. Battaglia et al. (2008), for instance, allow a metallicity gap of $-1.7 < {\rm [Fe/H]} < -1.5$. We therefore repeated our analysis, this time taking out one quarter of each subpopulation on both sides of the metallicity cut. The result may be seen in Fig. A2. We obtain $\Gamma = 1.59^{+0.44}_{-0.37}$ and $\lambda = 0.94^{+0.27}_{-0.19}$ for the Walker et al. (2009) estimator and $\lambda = 1.02^{+0.28}_{-0.21}$ for the Wolf et al. (2010) estimator when including the metallicity gap. This result is clearly consistent with our previous results for the Walker et al. (2009) and Wolf et al. (2010) estimators when a metallicity gap was not included (Section 3.2).

APPENDIX B

B1 Numerical convergence of galaxy properties

As mentioned in Section 2.2, we require that the galaxies in our sample include over 1000 stellar particles. Since the stellar particles are then split into two metallicity subpopulations, either or both of these subpopulations may end up with a number of particles too small for the properties such as $\kappa_{\rm rot}$ and the sphericity s, discussed in Section 2.4, to numerically converge. We therefore carry out the

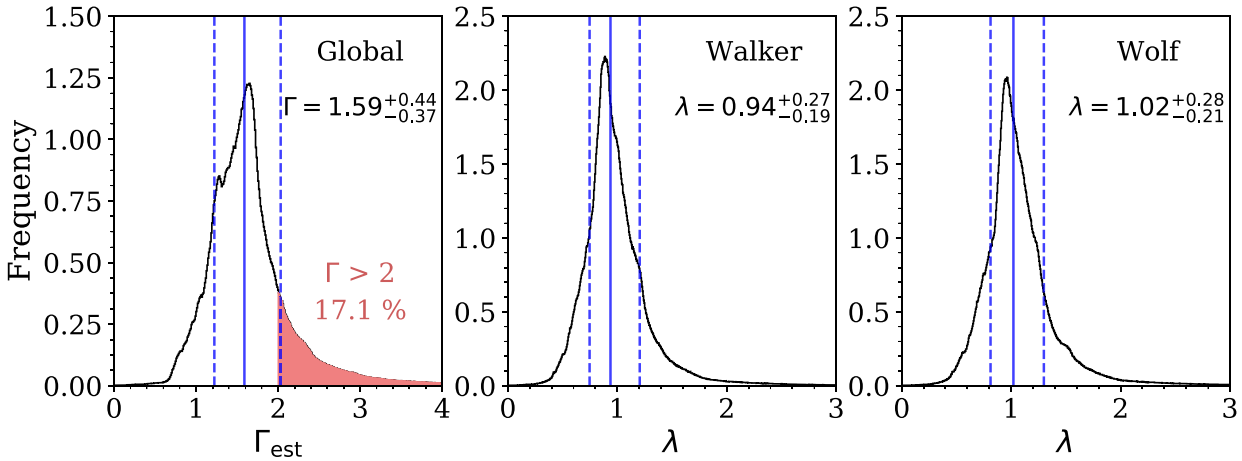

Figure A2. Overall distributions of estimated Γ_{est} (left) and λ for Walker et al. (2009) (middle) and Wolf et al. (2010) (right) estimators for galaxies in our sample when a metallicity gap is introduced between the two subpopulations, taking out a quarter of each subpopulation on either side of the metallicity cut. The distributions are consistent with our previous results (top panel of Fig. 10), suggesting that kinematic mixing between the subpopulations does not play a major role in the inferred distribution of slopes Γ.

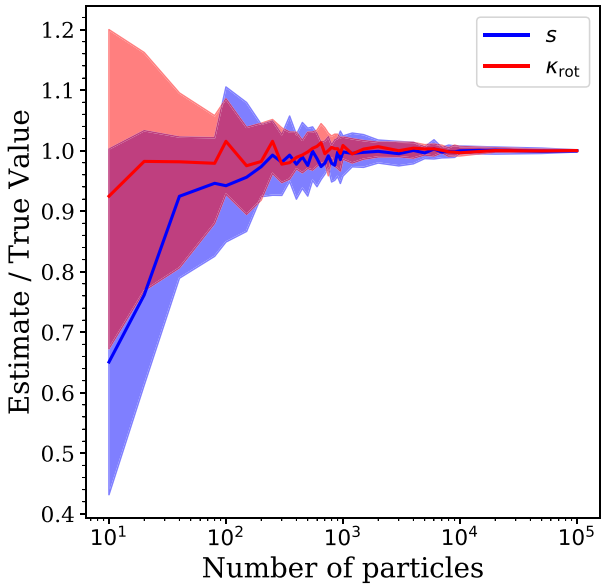

Figure B1. The accuracy of the estimates of sphericity s (blue) and κ_{rot} (red) as a function of the number of stellar particles with which they were calculated, shown for a sample of 37 dwarfs containing 10^5 to 10^6 stellar particles. The 'true' values are those calculated using all particles belonging to each galaxy. The blue and red bands represent 1σ scatter for s and κ_{rot}, respectively. Above a 1000 particles, the values are well converged and at ∼400 particles (the minimum number of particles belonging to a subpopulation in our sample of 50 galaxies) the estimates are, on average, accurate and the scatter is less than 10 per cent.

following test for convergence. We take a sample of 37 dwarfs with $10^5 - 10^6$ stellar particles from the five high-resolution APOSTLE volumes and we calculate the 'true' values of κ_{rot} and s, where we include all particles belonging to the galaxy as defined in Section 2.2. We then take progressively smaller particle samples and recalculate these properties. The result of this test may be seen in Fig. B1, where we show the accuracy of the estimates as a function of the number of particles with which they were calculated. It can be seen that the scatter in the estimate accuracy increases significantly for smaller particle subsamples. The median estimates of κ_{rot} are generally accurate, even for <100 stellar particles, while the sphericity, s, can be substantially underestimated.

In our sample of 50 dwarfs with two metallicity subpopulations, the minimum number of particles found in an individual subpopulation is just over 400. For this number of particles the estimates are generally accurate, with the 1σ scatter of about 5–10 per cent, as can be seen in Fig. B1. We thus conclude that the values of κ_{rot} and s presented in this work are not affected by the number of particles assigned to individual metallicity subpopulations to any significant extent.

This paper has been typeset from a TEX/LATEX file prepared by the author.